Journal of Materials Chemistry B

ROYAL SOCIETY OF CHEMISTRY

PAPER

View Article Online
View Journal

Cite this: DOI: 10.1039/d6tb00226a

In vitro models of oxidative stress, mitochondrial dysfunction, and inflammation for evaluation of neuroprotective biomaterials

Fucen Luo,[a] Thelma Akanchise,[a] Borislav Angelov[b] and Angelina Angelova *[a]

Received 28th January 2026,
Accepted 7th April 2026

DOI: 10.1039/d6tb00226a

rsc.li/materials-b

Neurodegenerative diseases arise from intertwined mechanisms involving oxidative stress, mitochondrial dysfunction, and neuroinflammation, leading to progressive neuronal loss. Developing *in vitro* models that reproduce these distinct yet interconnected pathological features is essential for evaluating neuroprotective biomaterials. In this work, differentiated SH-SY5Y neuronal-like cells were used to establish complementary stress-induced models reflecting oxidative, mitochondrial, and inflammatory injury. Lipopolysaccharide (LPS), rotenone (Rot), and oligomycin A (Oli) were systematically assessed to define conditions that elicit reproducible neuronal damage, using our potassium persulfate (KPS) oxidative stress model as a reference for redox-mitochondrial interactions. Quantitative enzymatic assays and ELISA-based analyses showed that LPS activated NF-κB and IL-1β signaling with mild oxidative stress. Rot modulated Nrf2 and SOD expression, and Oli depleted ATP synthase while suppressing GSH-Px. To evaluate the translational relevance of these models, monoolein-plasmalogen (MPL) lipid liquid crystalline nanoparticles (LCNPs) were studied as neuroprotective assemblies loaded with melatonin or quercetin. MPL LCNPs demonstrated intrinsic antioxidant and mitochondrial-stabilizing activity, restoring ATP synthase activity, reducing intracellular ROS, and attenuating LPS-induced NF-κB activation. The presented multi-model framework provides a robust platform for characterizing neuronal stress responses and supports the rational design of neuroprotective biomaterials for neuroengineering and regenerative medicine.

1. Introduction

Neurodegenerative diseases represent one of the most complex and unresolved challenges in medicine. They are marked by progressive neuronal loss arising from the interplay of oxidative stress, mitochondrial dysfunction, and chronic neuroinflammation.[1,2] These interconnected processes disrupt neuronal homeostasis, compromise bioenergetic balance, and activate programmed cell death pathways,[3] ultimately impairing neuronal survival, plasticity, and long-term repair. Designing biomaterials capable of preserving neuronal function and promoting regeneration, therefore, requires a mechanistic understanding of how these stressors interact to propagate degenerative processes.

In vitro neuronal models provide a controlled, reproducible platform for studying these mechanisms and evaluating therapeutic strategies. The human neuroblastoma SH-SY5Y cell line is widely used due to its robustness, reproducibility, and ability to differentiate into neuron-like cells.[4,5] Primary neuronal cultures offer superior physiological relevance but are limited by accessibility, lack of proliferation, and variability. In contrast, the SH-SY5Y model provides a scalable and reproducible alternative, albeit with reduced neuronal complexity.[5] Differentiated SH-SY5Y cells exhibit catecholaminergic features, including tyrosine hydroxylase activity, dopamine synthesis, and noradrenaline release,[6,7] making them particularly suitable for neurodegenerative processes relevant to diseases such as Parkinson's and Alzheimer's.[4,8] Their responsiveness to diverse neurotoxic stimuli and well-characterized signaling pathways further support their use in evaluating neuroprotective materials.

Different neurotoxic agents are commonly used to model specific aspects of neuronal injury, including oxidative stress, mitochondrial impairment, and inflammation.[9] In SH-SY5Y cells, oxidative stress, inflammation, or the pathological oxidative burden can be induced by hydrogen peroxide (H_2O_2), lipopolysaccharide (LPS), or 6-hydroxydopamine (6-OHDA),[10–13] respectively. Mitochondrial dysfunction is modeled using rotenone (Complex I inhibition) or oligomycin A (Complex V inhibition).[14,15] These stimuli promote reactive oxygen species (ROS) excessive generation

[a] Université Paris-Saclay, CNRS, Institut Galien Paris-Saclay, F-91400 Orsay, France. E-mail: angelina.angelova@universite-paris-saclay.fr
[b] Extreme Light Infrastructure ERIC, CZ-25241 Dolni Brezany, Czech Republic

and activate inflammatory pathways such as nuclear factor kappa B (NF-κB), mitogen-activated protein kinase (MAPK), and Janus kinase/signal transducer and activator of transcription (JAK/STAT) further impairs oxidative burden through the release of pro-inflammatory cytokines, including tumour necrosis factor-α (TNF-α), interleukin-1β (IL-1β), and interleukin-6 (IL-6).[14]

Neurodegenerative diseases are multifactorial, and commonly used *in vitro* single models capture only specific aspects of neurodegeneration. To address this limitation, combining complementary stress models provides a more comprehensive evaluation of neuronal injury, but still shares the general limitations of 2D cultures, including the lack of cellular complexity and tissue architecture.[15] More advanced *in vitro* systems, such as 3D cultures, brain organoids, and organ-on-chip, better reproduce *in vivo*-like environments, such as multicellular interactions and spatial organization.[16–18] However, these models are more complex, variable, and less suitable for high-throughput screening. Thus, multi-model 2D approaches can provide a more realistic and mechanistically grounded framework for screening neuroprotective candidates and guiding the development of biomaterials aimed at preserving neuronal function and promoting regeneration.

Lipid-based nanoparticles have drawn interest as versatile biomaterials for neurological applications owing to their biocompatibility, structural tunability, and ability to deliver therapeutic molecules in a controlled manner.[19–22] Their capacity to encapsulate antioxidants, anti-inflammatory agents, and mitochondrial stabilizers makes them strong candidates to counteract neuronal stress.[23] However, their evaluation requires reliable *in vitro* models that capture key features of neuronal stress.

To establish the utility of the developed neuronal stress models (LPS, Rot, and Oli), we employed them as *in vitro* experimental models (Fig. 1) for evaluating the efficacy of self-assembled lipid-based neuroprotective biomaterials composed of nonlamellar lipid monoolein-plasmalogen (MPL) mixtures (see Fig. 2A below). These liquid crystalline nanoparticles (LCNPs) exhibit a bicontinuous lipid membrane nanostructure that enables the encapsulation or co-encapsulation of hydrophobic (*e.g.*, melatonin [MT] and quercetin [Quer]) and hydrophilic neuroprotective agents. The nonlamellar cubic phase formed by the self-assembled MO/water matrix confers structural stability, while the incorporation of PUFA-rich plasmalogens enhances membrane organization and imparts both antioxidant and neuroprotective functions.[24]

The present work establishes a multi-model *in vitro* platform for the systematic evaluation of neuroprotective lipid nanomaterials, linking distinct stress mechanisms to biomaterial performance (Fig. 1). The rationale of the present study is grounded in the

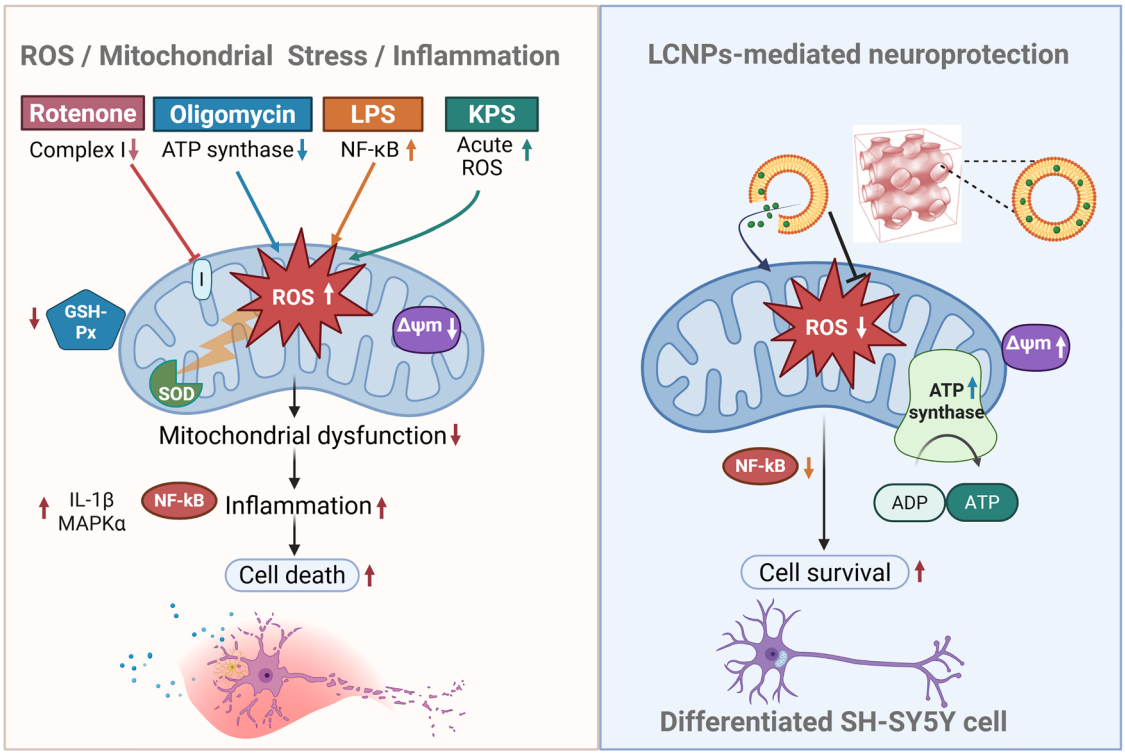

Fig. 1 Schematic presentation of cellular mechanisms involving reactive oxygen species (ROS), mitochondria-mediated oxidative stress, and inflammation in retinoic acid (RA)-differentiated SH-SY5Y neuronal-like cells, and possible protection by lipid-based cubosomal nanoparticle formulations. The left panel illustrates the induction of neuronal stress by multiple *in vitro* models, including rotenone (Complex I inhibition), oligomycin A (ATP synthase inhibition), LPS (NF-κB mediated inflammation), and KPS (acute oxidative stress), which collectively lead to excessive reactive oxygen species (ROS) production. Elevated ROS triggers mitochondrial dysfunction, characterized by decreased mitochondrial membrane potential (Δψm) and impaired antioxidant defences, ultimately promoting inflammation and cell death. The right panel demonstrates the protective effects of LCNPs, which attenuate oxidative stress by reducing ROS levels, restoring mitochondrial function, and enhancing ATP synthase activity. LCNPs treatment also suppresses NF-κB-mediated inflammatory signaling, thereby improving cell survival (Created with BioRender.com).

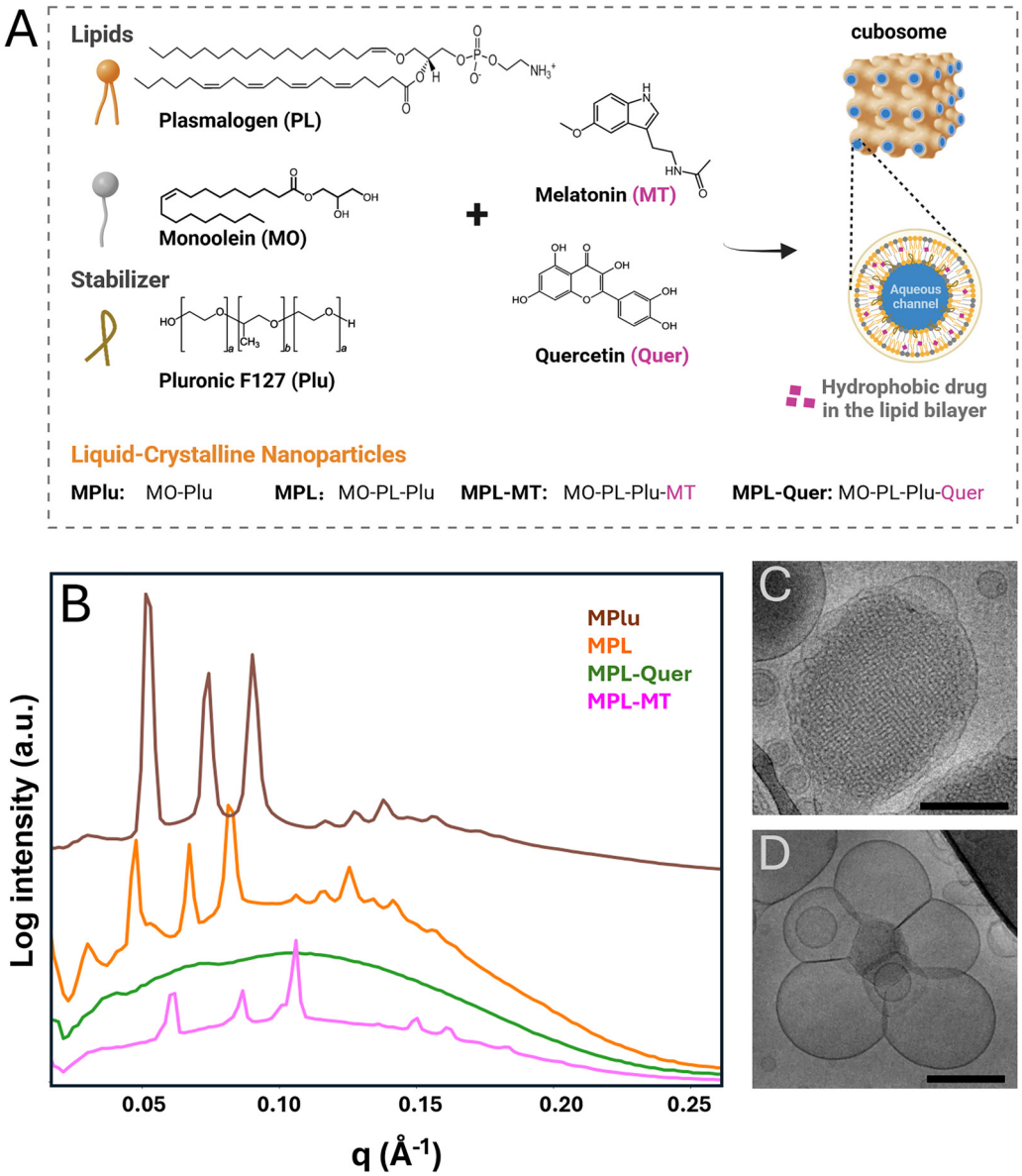

Fig. 2 Main constituents for the fabrication of monoolein (MO)-plasmalogen (PL) liquid-crystalline nanoparticles (cubosomes) by self-assembly (MO : PL, 1 : 2 w/w ratio) and their structural characterization. The antioxidants MT and Quer were incorporated at 5% or 2% of the MO lipid mass, respectively. MPL cubosomes were obtained by hydration and dispersion of an amphiphilic mixture of MO, PL, and Pluronic F127 (Plu) into LCNPs, allowing encapsulation of hydrophobic bioactives within the lipid bilayer domains of these LCNPs. The internal bicontinuous cubic phase structure provides aqueous nanochannel domains suitable for the loading of neuroprotective molecules. (Created with *BioRender.com*). (B) Small-angle X-ray scattering (SAXS) profiles of the different LCNP formulations showing characteristic Bragg peaks corresponding to an internal cubic phase structure (brown, orange, and pink plots). (C) and (D) Cryo-transmission electron microscopy (cryo-TEM) images of two representative LCNPs formulations. Panel (C) shows the inner cubic lattice arrangement of cubosome-type LCNP, while panel (D) displays vesicular membrane structures lacking long-range periodicity and coexisting with a small LCNP with a dense internal structure (small cubosome with diameter ~120 nm). Scale bar is 200 nm.

comparison of defined neuronal stress models, within which the therapeutic activity of multifunctional LCNPs is evaluated to establish an integrated *in vitro* platform that links oxidative and mitochondrial injury pathways to biomaterial-mediated neuroprotection. Incorporation of our previously validated KPS oxidative stress model[25] further enhances the translational relevance of this framework and supports the rational development of advanced *in vitro* testing strategies for neuroengineering, neuroprotection, and nerve-regeneration research.

2. Experimental section

2.1. Materials

Monoolein (MO, C18 : 1c9, purity ≥99%), melatonin (MT, purity >98%), Pluronic F127, retinoic acid (RA), quercetin (Quer), lipopolysaccharide (LPS), 2′,7′-Dichlorodihydrofluorescein diacetate (DCFH-DA), butylated hydroxytoluene (BHT), and (4,5-dimethylthiazol-2-yl)-2,5-diphenyltetrazolium bromide (MTT) were purchased from Sigma-Aldrich (Praha or Saint-Quentin). The scallop-derived

plasmalogen (PL), obtained from our previous work,[26] contained ethanolamine vinyl ether phospholipids (49.4%), choline vinyl ether phospholipids (24.9%), cholesterol (16.0%), and ceramide aminoethyl phosphonate (9.7%).[26] Oligomycin A (Oli, purity >95%) and rotenone (Rot, purity >95%) were purchased from Cayman Chemical (Ann Arbor, MI, USA). Milli-Q water (Millipore, Molsheim, France) was used to prepare phosphate buffer (NaH_2PO_4/Na_2HPO_4, 1×10^{-2} M, pH 7.0; using analytical-grade reagents, Merck). For cell culture studies, penicillin–streptomycin, phosphate-buffered saline (PBS), trypsin-EDTA, and MTT reagents were obtained from Sigma-Aldrich (Saint-Quentin-Fallavier, France). Gibco™ Dulbecco's Modified Eagle Medium (DMEM) with high glucose content and fetal bovine serum (FBS) were purchased from Thermo Fisher Scientific (Illkirch, France). Fluorescent dyes and staining kits were obtained from Thermo Fisher Scientific and Invitrogen.

2.2. Preparation of liquid crystalline lipid nanoparticles

LCNPs were prepared through the hydration of a lyophilized lipid film, followed by mechanical agitation and dispersion in an aqueous medium.[24,26] Specifically, lipids, surfactants (Plu), and either MT or Quer were precisely weighed and dissolved in chloroform according to the mass ratios listed in Table S1. The solution was vortexed to achieve uniform mixing, after which the solvent was gently evaporated under a nitrogen gas stream at room temperature for about 1 hour, forming a thin lipid film. The film was subsequently freeze-lyophilized overnight to eliminate any remaining solvent. For nanoparticle formation, the dried lipid film was hydrated with an aqueous phosphate buffer (1×10^{-2} M) containing BHT to prevent oxidation. The resulting mixture was then sonicated and vortexed, in cycles, in an ice bath for a total of 15 minutes to facilitate nanodispersion. Finally, the suspension was stored at 4 °C overnight to allow spontaneous self-assembly of liquid crystalline lipid nanoparticles such as cubosomes and hexosomes.[12,25,27]

2.3. Dynamic light scattering (DLS) measurements

The hydrodynamic diameters and size distribution of the LCNPs were measured by DLS using a Zetasizer Nano ZS90 (Malvern Instruments, UK). Samples were dispersed in excess aqueous medium and illuminated by a laser beam, with scattered light detected at a 90° angle. Measurements were performed in triplicate at 25 °C. The refractive index and viscosity of Milli-Q water were set to 1.330 and 0.8872 mPa s, respectively. Size distributions and polydispersity index (PDI) of LCNPs (MPlu, MPL, MPL-MT) are presented in SI (Fig. S1).

2.4. Small-angle X-ray scattering (SAXS)

SAXS experiments were conducted at the SWING beamline of the SOLEIL synchrotron (Saint-Aubin, France) following a protocol similar to that previously reported.[27] Dispersed nanoparticle suspensions were loaded into sealed X-ray capillaries and mounted on a custom holder equipped with (X, Y, Z) positioning control. Measurements were carried out at a constant temperature of 22 °C. The sample-to-detector distance was set to 2 m, and the incident X-ray beam on the sample had a spot of 25×375 μm^2. Scattering patterns were collected using a two-dimensional EigerX 4M detector (Dectris AG, Baden-Daettwil, Switzerland) at an energy of 12 keV, covering a scattering vector q-range of 0.00426–0.37 Å^{-1}. The X-ray wavelength was λ = 1.033 Å. Each acquisition was performed with an exposure time of 500 ms, and 10 individual measurements were averaged for each sample. Calibration of the q-range was achieved using silver behenate (d = 58.38 Å) as a standard reference. Data analysis was performed using the RAW software.

2.5. Cryogenic transmission electron microscopy (cryo-TEM)

Cryo-TEM analysis was performed as previously described.[24] In brief, a 2 μL droplet of the sample was applied onto a lacey carbon film-coated copper grid (Science Services, Munich, Germany) that had been hydrophilized by glow discharge for 30 s (Solarus, Gatan, Munich, Germany). Excess liquid was blotted away to create a thin aqueous film spanning the lace holes. The grid was then rapidly plunge-frozen in liquid ethane and cooled to 90 K using liquid nitrogen under controlled temperature and humidity conditions (Leica EM GP, Wetzlar, Germany). The vitrified sample was transferred to a cryo-transfer holder (CT3500, Gatan, Munich, Germany) and imaged using a Zeiss EM922 Omega energy-filtered transmission electron microscope (EFTEM) operated at 200 kV (Carl Zeiss Microscopy, Jena, Germany). Zero-loss energy-filtered images (ΔE = 0 eV) were recorded under low-dose conditions (100–1000 e^- nm^{-2}) with a bottom-mounted UltraScan 1000 CCD camera (Gatan, Munich, Germany) and processed using DigitalMicrograph GMS 1.9 software (Gatan, Munich, Germany). The investigated lipid nanoparticles exhibited sizes consistent with the thickness of the vitreous ice film, with no signs of deformation or flattening. Images were acquired close to or slightly under focus to improve contrast.

2.6. SH-SY5Y cell culture and differentiation

Differentiated human neuroblastoma SH-SY5Y cells were used as an *in vitro* neuronal model.[28] Cells were cultured in high-glucose DMEM, supplemented with 10% FBS and 1% penicillin–streptomycin at 37 °C in a humidified atmosphere containing 5% CO_2. Differentiation into a neuronal phenotype was induced by treating the cells with 10 μM RA for 5 days.

2.7. Morphological assessment

Differentiated SH-SY5Y cells were exposed to LPS, Rot, or Oli at predetermined concentrations to induce neuroinflammatory or neurotoxic conditions. Morphological alterations were observed using an OLYMPUS CKX53 microscope with a 10× objective after 24 h of exposure. Changes in cell body shape, neurite outgrowth, and cell density were compared with those of untreated controls to evaluate the extent of neuronal injury.

2.8. MTT assay of cell viability

Cell viability was quantified using the MTT colorimetric assay, which measures mitochondrial metabolic activity as an indirect indicator of cell viability and cytotoxicity. The assay relies on the reduction of the yellow MTT compound to insoluble purple formazan by NAD(P)H-dependent oxidoreductase enzymes in

viable cells. SH-SY5Y cells were seeded in 96-well plates at a density of 3.0×10^4 cells per well and differentiated with 10 μM RA for 5 days. Following differentiation, cells were treated with LPS, Rot, or Oli at different concentrations for 24 h. Cells maintained in FBS- and RA-free medium without treatment served as the control group.

After incubation, MTT reagent was added, and cells were maintained for 1 h at 37 °C. Formazan crystals were dissolved in DMSO, and absorbance was recorded at 570 nm using a microplate reader. The absorbance intensity correlated with the proportion of metabolically active cells.

2.9. Lactate dehydrogenase (LDH) release assay of cytotoxicity

LDH release was measured to assess cell membrane integrity as an indicator of cytotoxicity. Cytotoxicity was evaluated using the CytoSelect™ LDH Cytotoxicity Assay Kit (CBA-241, Cell Biolabs Inc., USA) according to the manufacturer's protocol. Human SH-SY5Y cells were seeded in 96-well plates at a density of 3×10^4 cells per well and differentiated with 10 μM RA for 5 days. After differentiation, cells were treated with LPS, Rot or Oli at the indicated concentrations. Following 24 h to 48 h of incubation at 37 °C in a humidified atmosphere containing 5% CO_2, cell-free supernatants were collected to assess LDH release. For each condition, the experimental wells contained the test compounds, while negative (untreated) and positive (Triton X-100–treated) controls were included. Briefly, 90 μL of supernatant from each well was transferred to a new 96-well plate, followed by the addition of 10 μL of LDH assay reagent. Plates were incubated at 37 °C for 30 min to 4 h, and absorbance was measured at 450 nm using a microplate reader. The percentage of cytotoxicity was calculated relative to maximum LDH release (positive control).

$$\%\,\text{Relative cytotoxicity} = \frac{\text{OD}_{\text{experimental}} - \text{OD}_{\text{negative}}}{\text{OD}_{\text{positive}} - \text{OD}_{\text{negative}}} \times 100$$

2.10. Intracellular ROS and mitochondrial membrane potential (ΔΨm) changes by flow cytometry detection

Flow cytometry was employed to assess oxidative stress and ΔΨm changes in RA-differentiated SH-SY5Y cells. Cells were seeded at a density of 3.0×10^5 cells per well in 6-well plates and differentiated with 10 μM RA for 5 days. After differentiation, cells were exposed to LPS, Rot, or Oli for 24 h, or to 50 mM KPS for 30 min, followed by treatment with 1 μM LCNPs (MPlu, MPL, or MPL-Quer) or an equivalent concentration of free Quer for 24 h.

Intracellular reactive oxygen species (ROS) levels were quantified by flow cytometry using 10 μM DCFH-DA as a fluorescent probe. Cells were incubated with DCFH-DA for 30 min at 37 °C, washed twice with PBS, and analyzed using a BD Accuri C6 flow cytometer (Ex 488 nm/Em 533 nm, FL-1A channel). The relative fluorescence intensity of treated cells was normalized to untreated controls (FBS-free medium), representing background intracellular ROS generation.

For ΔΨm determination, cells were harvested after cell exposure to KPS and subsequent LCNPs or free Quer treatment, washed with PBS, and resuspended in 100 μL JC-10 dye loading solution. After 15 min incubation at room temperature, fluorescence was measured on the BD Accuri C6 flow cytometer. Green fluorescence (JC-10 monomers) was detected at Ex 488 nm/Em 530 nm (FL-1) and red fluorescence (JC-10 aggregates) at Ex 488 nm/Em 578 nm (FL-2). In polarized mitochondria, JC-10 forms red aggregates, while depolarized mitochondria exhibit green monomer fluorescence.[29] Changes in ΔΨm were expressed as the red-to-green fluorescence ratio [FL-2/FL-1], indicating relative mitochondrial polarization status.[30]

2.11. Mitochondrial Complex V (ATP synthase) activity assay

The activity of mitochondrial Complex V (ATP synthase) in differentiated SH-SY5Y cells was evaluated using the MitoTox™ Complex V OXPHOS Activity Assay Kit (ab109907, Abcam, UK) following the manufacturer's protocol. Cells were seeded in 75 cm^2 flasks at a density of 8×10^6 cells, differentiated with 10 μM RA for 5 days, and then exposed to 0.5 μM Oli to inhibit ATP synthase. To investigate the protective and restorative effects of desired formulations, cells were either pre-treated (before Oli exposure) or post-treated (after Oli exposure) with 1 μM free MT or MT-loaded MPL-MT NPs for 24 h. Following treatment, cells were lysed, and mitochondria were isolated using the Mitochondria Isolation Kit (ab110171, Abcam, UK) with a Dounce homogenizer. ATP synthase activity was determined by measuring the rate of NADH oxidation at 340 nm using a microplate reader. Results were expressed as relative ATP synthase activity normalized to untreated control cells.

2.12. Determination of Nrf2 and SOD levels, and GSH-Px activity in SH-SY5Y cell lysates

The antioxidant defense response of differentiated SH-SY5Y cells was evaluated by quantifying nuclear factor erythroid 2-related factor 2 (Nrf2), superoxide dismutase (SOD), and glutathione peroxidase (GSH-Px) activities using commercial ELISA-based assay kits according to the manufacturers' instructions. Cells were seeded in 75 cm^2 flasks at a density of 6×10^6, differentiated with 10 μM RA for 5 days, and subsequently exposed to oxidative stress inducers as specified below.

Nrf2 protein levels were measured using the Human Nrf2 ELISA Kit (ab277397, Abcam, UK). Cells were treated with 1 μg mL^{-1} LPS, 2.5 μM Oli, or 5 μM Rot for 24 h, or with 50 mM KPS for 30 min, followed by incubation in FBS/RA-free medium for 24 h. This sandwich ELISA uses Nrf2-specific capture and HRP-conjugated detection antibodies, and colorimetric development with TMB substrate, measured at 450 nm. Absorbance intensity is proportional to Nrf2 concentration in the sample.

SOD protein levels were quantified using the Human Cu/Zn SOD ELISA Kit (ab119520, Abcam, UK) under identical treatment conditions. The assay employs Cu/Zn SOD-specific antibodies pre-coated on 96-well plates and HRP-TMB colorimetric detection at 450 nm. This kit is specific to the SOD1 Cu/Zn isoform. Functionally, SOD catalyzes the dismutation of superoxide radicals ($O_2^{-\bullet}$) into oxygen and H_2O_2, thus protecting cells from oxidative damage.

GSH-Px activity was assessed using the GSH-Px Assay Kit (Cat. No. 703102, Cayman Chemical, Ann Arbor, MI, USA). Cells were treated with 0.5 μM Oli or 0.5 μM Rot for 24 h, or with 50 mM KPS for 30 min followed by incubation in FBS/RA-free medium for 24 h. After treatment, cells were lysed with CelLytic™ M buffer (Cat. No. C2978, Sigma-Aldrich) and centrifuged at 1500 g for 15 min at 4 °C to collect supernatants. GSH-Px activity was determined through a coupled reaction with glutathione reductase, in which H_2O_2 is reduced by GSH-Px using reduced glutathione. The concurrent oxidation of NADPH to $NADP^+$, recorded as a decrease in absorbance at 340 nm, reflects GSH-Px enzymatic activity.

Collectively, Nrf2, SOD, and GSH-Px measurements provided complementary indicators of the intracellular antioxidant defense capacity and its regulation in SH-SY5Y cells under oxidative stress.

2.13. Determination of IL-1β, p38 MAPKα/MAPKα, and NF-κB expression levels in SH-SY5Y cell lysates

Inflammatory pathway activation in differentiated SH-SY5Y cells was assessed by quantifying IL-1β, MAPKα, and NF-κB expression levels using commercial ELISA kits according to the manufacturers' instructions. Cells were seeded in 75 cm^2 flasks at a density of 6×10^6, differentiated with 10 μM RA for 5 days, and subsequently treated with LPS (0.5–10 μg mL^{-1}), Oli (0.5–2.5 μM), or Rot (1–5 μM) for 24 h, or with 50 mM KPS for 30 min, followed by incubation in FBS-free medium for 24 h.

MAPKα (pT180/Y182) and total MAPKα levels were quantified using the p38 MAPKα (pT180/Y182) and Total Simple Step ELISA® Kit (ab221013, Abcam, UK). This dual ELISA simultaneously detects phosphorylated and total MAPKα proteins *via* specific capture and HRP-conjugated detection antibodies. Colorimetric development using TMB substrate was measured at 450 nm, and the ratio of phosphorylated to total MAPKα was used to indicate MAPK activation.

NF-κB and IL-1β expression levels were determined using the corresponding Human NF-κB ELISA and Human IL-1β ELISA kits (Abcam, UK). Each assay employs antigen-specific capture and detection antibodies, and absorbance was read at 450 nm following the addition of TMB substrate and stop solution.

2.14. Total protein quantification by Bradford assay

Total protein concentration in cell lysates was determined using the Bradford Protein Assay in a 96-well plate format. A bovine serum albumin (BSA) stock solution (2 mg mL^{-1} in PBS) was prepared to generate a seven-point calibration curve for quantification. For each well, 5 μL of either BSA standard or cell lysate sample was mixed with 195 μL of Bradford reagent (Sigma-Aldrich, Cat. No. B6916-500ML). Absorbance was measured at 595 nm using a microplate reader, with blank correction applied. The calculated protein concentrations were used to normalize the expression data for Nrf2, SOD, GSH-Px, IL-1β, MAPKα, and NF-κB, ensuring consistent comparison across samples.

2.15. Data analysis

Data were analysed using GraphPad Prism (version 8.0.1). Results are presented as mean ± standard deviation (SD). Statistical differences among groups were evaluated using one-way ANOVA. A $p < 0.05$ was considered statistically significant.

3. Results and discussion

3.1. Structure characterization of liquid crystalline lipid nanoparticles by SAXS and Cryo-TEM

Synchrotron small-angle X-ray scattering (SAXS) measurements were performed to characterize the nanostructural organization of the designed multifunctional liquid crystalline lipid nanoparticles (LCNPs). Fig. 2B shows the SAXS patterns of the self-assembled LCNPs recorded at 22 °C. The blank cubosome formulation (MPlu), the plasmalogen-containing LCNPs (MPL), and the melatonin-loaded LCNPs (MPL-MT) all displayed well-resolved Bragg reflections indicative of long-range ordered lipid bilayer membrane organization. These reflections appeared at q-vector positions with spacing ratios of $\sqrt{2}$: $\sqrt{4}$: $\sqrt{6}$: $\sqrt{8}$: $\sqrt{10}$: $\sqrt{12}$: $\sqrt{14}$: $\sqrt{16}$, corresponding to the (110), (200), (211), (220), (310), (222), (321), and (400) Miller indices. Such patterns are characteristic of a cubic lipid phase with the *Im3m* space group symmetry (brown, orange, and pink plots in Fig. 2B). The Bragg peaks of the melatonin-loaded nanocarriers (MPL-MT) were weaker compared to those of the blank (MPlu) and plasmalogen-only (MPL) lipid dispersions. This reduction in intensity may arise from a decrease in electron density contrast between lipid domains and aqueous channels upon melatonin incorporation. The calculated cubic lattice parameter for the empty cubosomes (MPlu) was $a_{Q(Im3m)}$ = 17.01 nm. Incorporation of plasmalogen increased the lattice parameter to $a_{Q(Im3m)}$ = 18.83 nm. In contrast, encapsulation of MT (at 5% loading) resulted in a notable reduction of the cubic unit cell parameter to $a_{Q(Im3m)}$ = 14.56 nm. This can be attributed to the lipophilic nature of MT, which partitions between the hydrophobic core of the lipid bilayer and the lipid/water interfaces, thus modifying the negative spontaneous curvature and the water channel sizes. The decrease in $a_{Q(Im3m)}$ is consistent with MO partitioning into the lipid bilayer, leading to tighter packing and a reduced aqueous channel size. At variance, Quer-loaded LCNPs displayed broader scattering features, indicative of lower curvature and the lack of long-range ordered structure. This suggests the prevalence of vesicular membranes rather than a well-defined periodic cubic phase.

Cryogenic transmission electron microscopy (cryo-TEM) images reveal distinct internal nanostructures within the lipid nanoparticles (Fig. 2C and D). The nonlamellar lipid particles exhibited a highly ordered internal pattern characterized by a periodic lattice arrangement consistent with an inner cubic phase structure (Fig. 2C). The presence of regularly spaced, repeating domains indicates long-range internal organization, in accordance with the SAXS results evidencing the formation of *Im3m* cubic structure. In contrast, the SAXS pattern lacking

well-resolved Bragg peaks correlated with the formation of homogeneous spherical vesicular structures coexisting with small particles with denser interiors (Fig. 2D).

3.2. Cellular model of mitochondrial dysfunction induced by Rot or Oli in differentiated SH-SY5Y cells

3.2.1. Rot- or Oli-induced viability decrease and associated morphological changes in injured differentiated SH-SY5Y cells. To understand the contributions of ROS-mediated oxidative damage and mitochondrial dysfunction to neuronal injury, we employed Rot and Oli, two mitochondrial inhibitors with distinct mechanisms of action and ROS-inducing profiles. Rot disrupts the mitochondrial Complex I, causing ROS overproduction,[31] whereas Oli inhibits ATP synthase, leading to ATP depletion and indirect ROS induction.[32] Unlike the KPS-stress model, which directly induces acute oxidative stress in SH-SY5Y cells,[25] these neurotoxic agents enable the selective modelling of either oxidative or mitochondrial dysfunction, allowing for the differentiation of stress-specific neuronal responses.

First, we evaluated the viability of differentiated SH-SY5Y cells after exposure to mitochondrial inhibitors (Oli and Rot), assessed using the MTT assay. We observed that the differentiated cells cultured in medium containing 10% FBS after 5 days of RA treatment (RA/FBS(+) exhibited robust metabolic activity (100% viability). As shown in Fig. 3A, treatment with increasing concentrations (0.1–10 μM) of Oli or Rot for 24 h resulted in a concentration-dependent decrease in cell viability. At comparable concentrations, Oli caused a stronger inhibition of metabolic activity than Rot, with 10 μM Oli reducing viability from 80.5% to 30.8%.

Morphological examination under light microscope further supported these findings (Fig. 3B). Rot-treated cells displayed pronounced neurite retraction, soma shrinkage, and loss of neuronal network connectivity even at concentrations as low as 0.5 μM. This effect is consistent with mitochondrial Complex I inhibition leading to ATP depletion and enhanced oxidative damage, associated with increased protein carbonyl formation.[33] In contrast, cells exposed to low to moderate concentrations of Oli ($\leq$2.5 μM) preserved neuronal cell morphology, whereas at higher concentrations, subtle soma rounding, partial neurite shortening, and reduced cell density were observed.

3.2.2. Rot- or Oli-induced cytotoxicity and oxidative stress in differentiated SH-SY5Y cells. We next assessed the extent of mitochondrial stress-induced cytotoxicity and oxidative damage by measuring LDH release and ROS production in differentiated SH-SY5Y cells exposed to Rot or Oli. The results in Fig. 4A show that LDH release increased in a concentration and time-dependent manner following Rot treatment, whereas Oli required higher concentrations to produce comparable membrane damage. Rot significantly increased LDH release at lower concentrations (0.25–5 μM) after 24 h (Fig. 4A).

In contrast, Oli treatment induced a significant membrane damage at higher concentrations (5–20 μM) compared to Rot (Fig. 4B). At 5 μM, LDH release was only slightly elevated, whereas at 10 μM, LDH release increased markedly to over 50%, consistent with the MTT assay results, indicating substantial cytotoxicity toward SH-SY5Y cells at the studied concentration. Fig. 4C compares the effects of prolonged exposure of SH-SY5Y cells to Rot and Oli (0.5 μM, 48 h). Under these conditions, Rot markedly increased LDH release, while Oli did not significantly alter LDH levels.

We further evaluated intracellular ROS levels using DCF fluorescence. As shown in Fig. 4D, Oli treatment induced a dose-dependent increase in ROS production in SH-SY5Y cells. The elevation in ROS levels after 24 h exposure was more

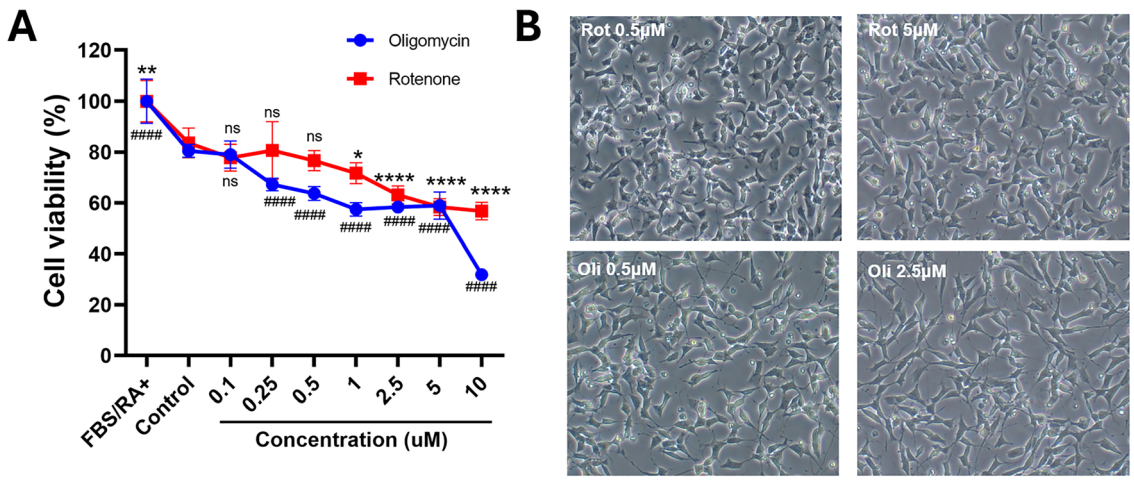

Fig. 3 Cell viability and morphological alterations induced by mitochondrial inhibitors in differentiated SH-SY5Y cells. (A) Differentiated SH-SY5Y cells were challenged with increasing concentrations (0.1-10 μM) of Oli or Rot for 24 h. Cell viability was evaluated by MTT assay, showing a significant reduction in metabolic activity at $\geq$0.25 μM Oli and $\geq$1 μM Rot, with pronounced cytotoxicity observed at 10 μM Oli compared with the untreated control (FBS/RA-). (B) Representative micrographs illustrating the morphological changes following treatment with different concentrations of Oli and Rot. Rot markedly reduced neurite length and induced cell-body shrinkage already at a low concentration (0.5 μM). Data in (A) are presented as mean ± SD (n = 6). Statistical significance was determined by one-way ANOVA; *p < 0.05, **p < 0.01, ****p < 0.0001 *vs.* control; ####p < 0.0001 *vs.* control; ns, not significant.

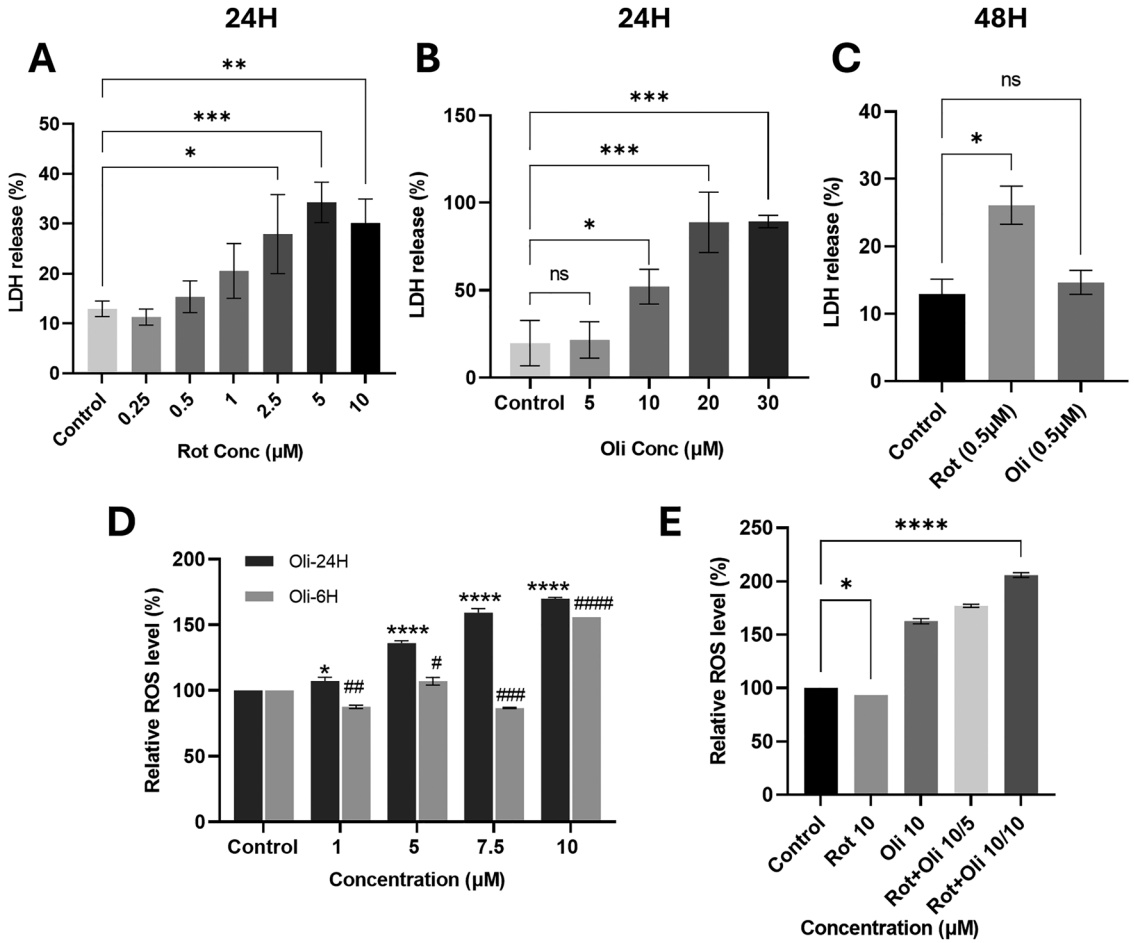

Fig. 4 Cytotoxicity and intracellular ROS levels induced by mitochondrial inhibitors in differentiated SH-SY5Y cells. (A) and (B) LDH release assays demonstrating a concentration-dependent increase in membrane damage caused by Oli or Rot after 24 h of exposure, with significantly elevated LDH release detected at 2.5 μM Rot and 10 μM Oli. (C) LDH release rates after 48 h exposure show a significant increase with 0.5 μM Rot compared with the control, whereas 0.5 μM Oli does not cause any notable change. (D) Relative ROS levels after treatment with different concentrations of Oli (1–10 μM) for 6 h and 24 h. (E) Relative ROS levels following treatment with 10 μM Rot, 10 μM Oli, and their combinations Rot + Oli 10/5 or Rot + Oli 10/10 (10 μM Rot+ 5 μM Oli or 10 μM Rot+ 10 μM Oli). Data are expressed as mean ± SD (n = 2 biological replicates). Statistical significance was determined by one-way ANOVA; *$p < 0.05$, **$p < 0.01$, ***$p < 0.001$, ****$p < 0.0001$ *vs.* control; #$p < 0.05$, ##$p < 0.01$, ###$p < 0.001$, ####$p < 0.0001$ *vs.* control; ns, not significant.

pronounced than that observed after 6 h, indicating a time-dependent accumulation of oxidative stress following mitochondrial ATP synthase inhibition. This result is consistent with the established mechanism of Oli, which impairs mitochondrial electron transport and promotes reactive oxygen species generation.[32] Treatment with 10 μM Rot alone for 24 h did not significantly increase ROS levels. However, co-treatment with Oli (Fig. 4E) markedly induced ROS production. Combined treatments (10 μM Rot + 5 μM Oli or 10 μM Rot + 10 μM Oli) resulted in the highest ROS generation, significantly exceeding the effects of each neurotoxic agent alone. These findings suggest a synergistic impairment of mitochondrial respiration, leading to excessive oxidative stress and disruption of redox homeostasis. Such a model of severe oxidative stress may cause extensive cell death, making it unsuitable for evaluating the recovery effects of bioactive materials or nanoformulations on mitochondrial dysfunction. Of note, a combination of 30 μM Rot and 10 μM Oli has been previously used to evaluate the protective effect of galantamine and MT against oxidative stress in SH-SY5Y neuroblastoma cells.[34]

It can be deduced that the observed outcomes reflect the distinct mechanisms of the studied inhibitors. Rot inhibits mitochondrial Complex I, leading to electron leakage and delayed oxidative stress, which primarily affects cytoskeletal stability and neurite morphology, with relatively modest early metabolic impairment. In contrast, Oli directly inhibits ATP synthase (Complex V), causing rapid ATP depletion and metabolic collapse, while morphological changes are less pronounced at moderate concentrations. The different LDH results further support these distinctions: Rot-mediated damage is delayed and concentration-sensitive at low doses, whereas Oli triggers immediate energy-dependent metabolic impairment with minimal early membrane disruption.

For identical cell culture conditions, Oli exerted a stronger inhibitory effect on cellular bioenergetic metabolism, whereas Rot caused more pronounced alterations in neurite morphology

and membrane integrity at lower concentrations. Understanding these differences is critical for selecting appropriate *in vitro* stress models when evaluating neuroprotective lipid nanoparticles, as distinct inhibitors may reveal complementary aspects of neuronal vulnerability.

3.3. Cellular model of oxidative stress-mediated inflammation induced by LPS in differentiated SH-SY5Y cells

3.3.1. LPS-induced morphological changes and viability reduction in differentiated SH-SY5Y cells.. Oxidative and metabolic dysfunction often leads to neuroinflammation in neurodegenerative disorders. To investigate this interrelated mechanism, we employed LPS as an inflammatory stimulus. We selected LPS because Rot and Oli are mitochondrial inhibitors that primarily induce oxidative and mitochondrial stress, respectively. While both agents disrupt mitochondrial function, their effects are largely confined to intracellular metabolic and redox pathways. In contrast, LPS activates neuroinflammatory signaling cascades through Toll-like receptor 4 (TLR4) engagement, triggering cytokine production (*e.g.*, TNF-α, IL-6, and IL-1β), and secondary oxidative stress in neuronal cells.[35–38]

Here, the cellular morphology assessment of SH-SY5Y cells following LPS stimulation was done at different concentrations in differentiated SH-SY5Y cells. Undifferentiated SH-SY5Y cells observed one day after seeding displayed typical polygonal morphology with short neurite extension (Fig. 5A). However, exposure to RA for 5 days (Fig. 5B) led to the development of elongated neurites and a differentiated neuronal phenotype.[39] Furthermore, SH-SY5Y cells were treated with increasing concentrations of LPS (0.5–40 μg mL^{-1}) to establish an inflammatory stress model.[40] At lower concentrations (0.5–10 μg mL^{-1}; Fig. 5C–E), cells retained their overall morphology with only minor signs of stress, such as slight neurite shortening and reduced cell density. However, at higher concentrations (20 and 40 μg mL^{-1}; Fig. 5F and 5G), the cells exhibited signs of stress, including reduced cell density accompanied by extensive cell rounding, fragmentation, and loss of neurite networks. This demonstrated severe cytotoxicity and cell death. Furthermore, MTT-assay results revealed a dose-dependent decrease in cell

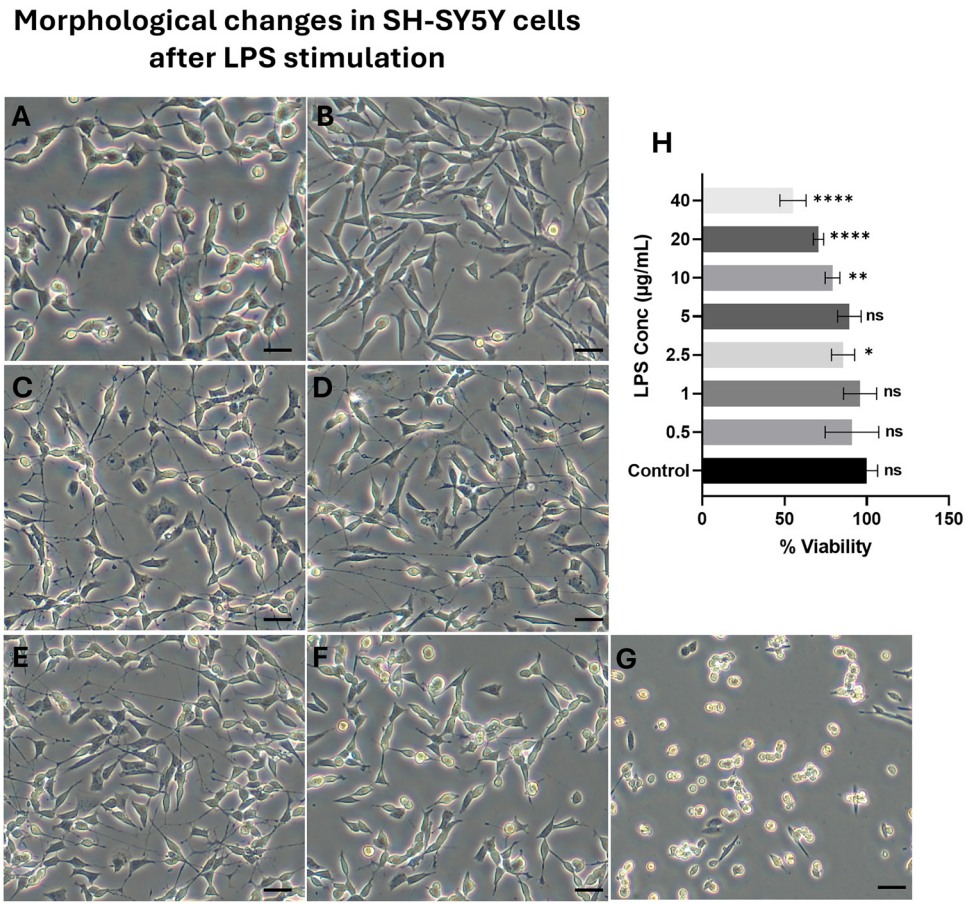

Fig. 5 Morphological changes and viability of differentiated SH-SY5Y cells after LPS stimulation. (A) Morphology of SH-SY5Y cells one day after seeding. (B) Cells differentiated for five days with retinoic acid (RA) display extended neurites and neuronal-like morphology. (C)–(G) Morphological changes following exposure to increasing concentrations of LPS (0.5, 1, 10, 20, and 40 μg mL^{-1}) for 24 h, and revealing a dose-dependent reduction in neurite length, cell body shrinkage, and detachment, with severe rounding and loss of cell integrity at higher concentrations. (H) Cell viability quantified using the MTT assay, showing a significant decrease in metabolic activity at ≥2.5 μg mL^{-1} LPS, with pronounced cytotoxicity at 20 μg mL^{-1} and 40 μg mL^{-1} (n = 6, * p = 0.036, ** p = 0.0011, **** $p < 0.0001$).

viability. A significant decrease in cell viability was detected at concentrations of 2.5 μg mL^{-1}, with the most substantial reductions observed at 20 μg mL^{-1} and 40 μg mL^{-1} (Fig. 5H). These results indicated that high-dose LPS stimulation can induce inflammatory stress accompanied by neuronal damage in differentiated SH-SY5Y cells.

3.3.2. LPS-induced cytotoxicity and oxidative stress in differentiated SH-SY5Y cells. To assess the cytotoxic and oxidative effects of LPS stimulation in differentiated SH-SY5Y cells, LDH release and intracellular ROS generation were quantified. As shown in Fig. 6A, LPS exposure led to a concentration-dependent increase in LDH release, indicating membrane damage and cytotoxicity. Compared with the control (FBS-free medium), a significant increase in LDH activity was observed already at low LPS concentrations (0.5–1 μg mL^{-1}), with cytotoxicity further elevated at higher doses (20–80 μg mL^{-1}). The sharp rise at 80 μg mL^{-1} suggested extensive membrane disruption and necrotic cell death under high inflammatory stress.

To further determine whether LPS-induced cytotoxicity was associated with oxidative stress, we evaluated intracellular ROS levels measured using DCF fluorescence. We observed that the exposure of SH-SY5Y cells to low LPS concentrations (0.1–1 μg mL^{-1}) caused a significant elevation in ROS levels compared to the control (Fig. 6B). Similarly, high LPS doses (10–160 μg mL^{-1}) induced a significant and sustained increase in ROS production (Fig. 6C). The results show that LPS triggers oxidative stress and cytotoxicity in a dose-dependent manner and therefore can serve as a suitable neurotoxic agent for modelling inflammation-mediated neuronal injury in SH-SY5Y cells.

It can be deduced that while Rot and Oli elicited complementary signaling cascades involving ROS generation and mitochondrial dysregulation, LPS provides a means to model the neuroinflammatory processes characteristic of neurodegenerative pathology.

3.4. Activation of IL-1β, MAPKα, and NF-κB signaling by LPS, Rot, and Oli in differentiated SH-SY5Y cells

Inflammatory responses were subsequently assessed by quantifying IL-1β expression, MAPKα phosphorylation, and NF-κB

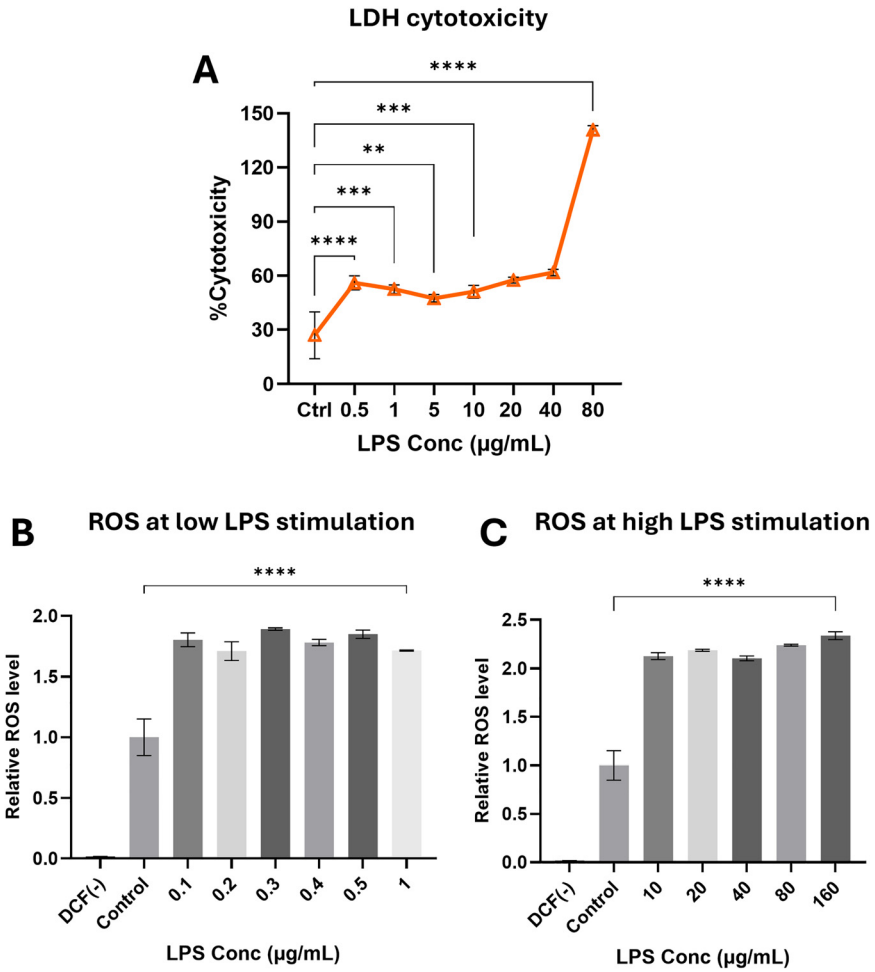

Fig. 6 LPS-induced cytotoxicity and ROS generation in differentiated SH-SY5Y cells. (A) LDH assay showing a dose-dependent increase in cytotoxicity following LPS stimulation (0.5–80 μg mL^{-1}) for 24 h. Data are presented as mean ± SD (n = 3, **** $p < 0.0001$, *** $p < 0.001$, ** $p < 0.01$ *vs.* control). (B) and (C) Intracellular ROS levels at low (0.1–1 μg mL^{-1}) and high LPS concentrations (10–160 μg mL^{-1}), measured by DCF fluorescence dye. Data are presented as mean ± SD (n = 2, biological replicates) **** $p < 0.0001$ *vs.* control.

levels (Fig. 7). These mediators are functionally interconnected, as IL-1β can activate MAPK signaling, which in turn promotes NF-κB translocation and the amplification of pro-inflammatory gene expression.[41] LPS treatment resulted in an increase in IL-1β levels, with significant upregulation observed at 5 and 10 μg mL^{-1} compared with control cells. In contrast, both Oli (2.5 μg mL^{-1}) and Rot (5 μg mL^{-1}) did not cause significant changes in IL-1β expression (Fig. 7A). The analysis of p38 MAPKα levels revealed no significant changes across treatments (Fig. 7B). To determine whether the tested neurotoxins induce inflammatory signaling, NF-κB activation was evaluated following exposure to LPS, Oli, or Rot. LPS significantly elevated NF-κB expression levels at all tested concentrations (0.5, 1, and 2.5 μg mL^{-1}) (Fig. 7C). In contrast, neither Rot nor Oli induced a significant change in NF-κB levels compared with untreated controls (Fig. 7D and E). These results confirmed that mitochondrial inhibitors primarily trigger oxidative rather than inflammatory responses.

3.5. Comparison of LPS, Oli, and Rot-induced antioxidant defense and inflammatory responses in differentiated SH-SY5Y cells

Having established that LPS primarily activates inflammatory signaling while Rot and Oli induce oxidative and mitochondrial stress, we next examined how these stimuli influence antioxidant defense mechanisms. To this end, differentiated SH-SY5Y cells were treated with LPS, Oli, or Rot, and changes in Nrf2 protein expression together with downstream enzymatic antioxidant responses, including superoxide dismutase (SOD) and glutathione peroxidase (GSH-Px), were analyzed and compared with responses observed in our previously established KPS-induced oxidative stress model (Fig. 8).

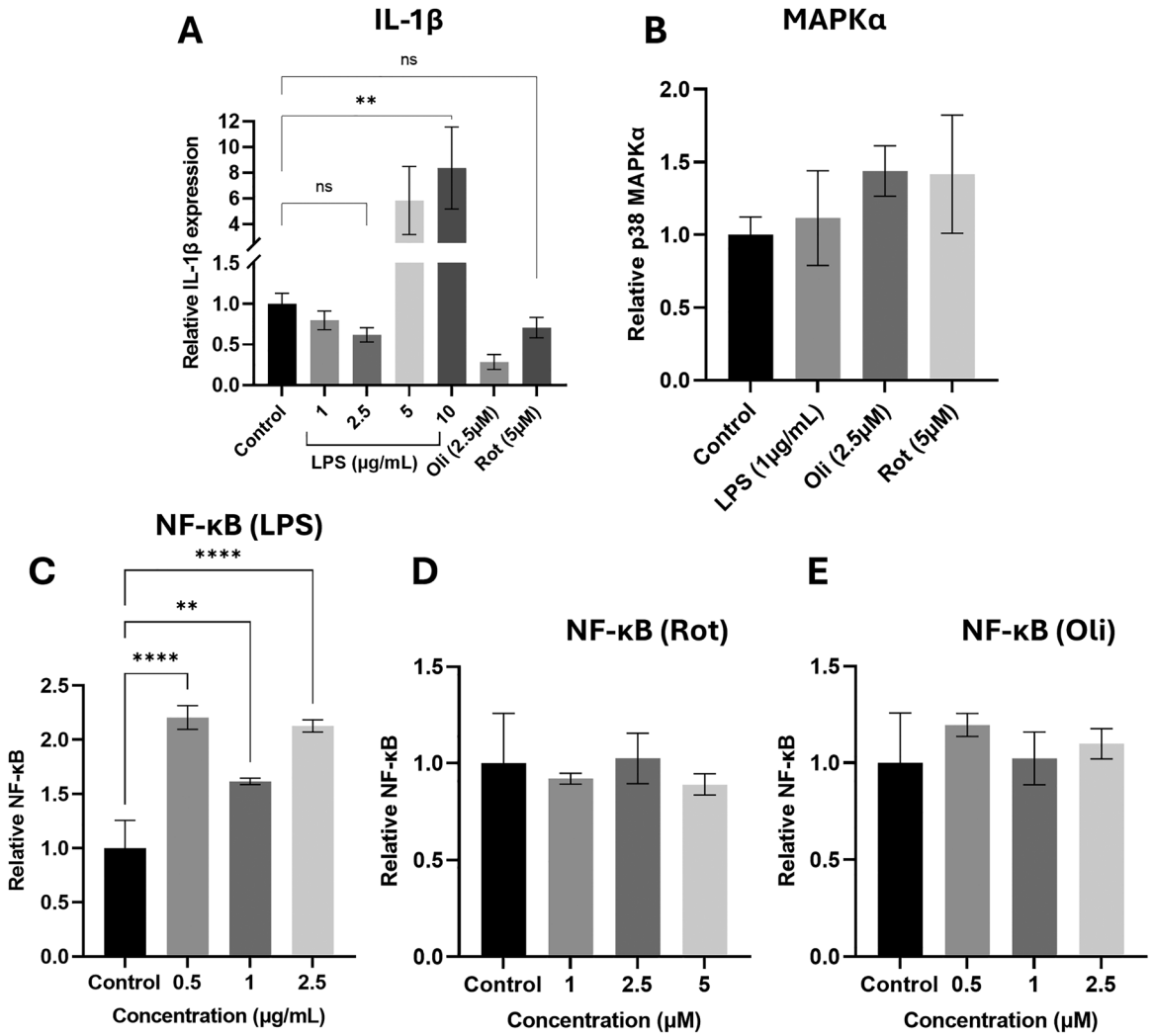

Fig. 7 Effects of LPS, Oli, and Rot on inflammatory signaling pathways in differentiated SH-SY5Y cells. (A) LPS induces an increase in IL-1β expression, with a significant rise at 5 and 10 μg mL^{-1}, whereas both Oli and Rot cause no significant changes (n = 2, ** $p < 0.05$ *vs.* control). (B) Relative phosphorylation of p38 MAPKα *vs.* total MAPKα expression in SH-SY5Y cells treated with LPS, Rot, and Oli for 24 h (n = 2, * $p = 0.0057$ *vs.* control). (C) Significantly increased NF-κB levels upon LPS stimulation. (D) and (E) Rot (1–5 μg mL^{-1}) and Oli (0.5–2.5 μg mL^{-1}) treatments for 24h did not cause significant changes in NF-κB expression levels, respectively. Data are expressed as mean ± SD (n = 3 biological replicates). Statistical significance was determined by one-way ANOVA; **$p < 0.01$, ***$p < 0.001$, ****$p < 0.0001$ *vs.* control; ns, not significant.

As shown in Fig. 8A, Rot treatment caused a significant Nrf2 expression (p = 0.0057), whereas LPS and Oli induced a slight elevation in Nrf2 levels. Regarding antioxidant enzymes, the relative SOD levels were elevated after 24 h exposure to LPS or Rot, while exposure to Oli or KPS (50 mM, 30 min) had no significant effect (Fig. 8B). The antioxidant GSH-Px enzymatic activity exhibited a distinct trend (Fig. 8C). A slight but non-significant decrease in GSH-Px activity was observed in Rot-treated cells (0.5 μM, 24 h; p = 0.095), whereas exposure to 0.5 μM Oli caused a pronounced reduction in GSH-Px activity (p = 0.0029). The highest suppression was observed in KPS-induced SH-SY5Y cells after 30 min of exposure to 50 mM, indicating impairment of the GSH-Px system ($p < 0.0001$).

Collectively, the obtained results suggest that Rot-induced mitochondrial Complex I inhibition appears to be associated with increased Nrf2 protein and SOD expression, supporting a compensatory antioxidant response. In contrast, ATP synthase inhibition by Oli appears to compromise GSH-Px activity without substantially elevating Nrf2 protein levels. Furthermore, KPS-induced oxidative stress selectively impaired the GSH-Px system. These findings highlight distinct oxidative stress adaptation mechanisms in SH-SY5Y cells. LPS triggers inflammatory and mild oxidative responses, Rot selectively induces Nrf2-mediated antioxidant responses, and Oli and KPS lead to specific depletion of GSH-Px activity. The latter reflects distinct mechanisms of oxidative stress and redox imbalance. These outcomes demonstrate the enzyme-specific sensitivity of neuronal cells to diverse mitochondrial and inflammatory stimuli, which is essential for elucidating neurotoxin-induced oxidative damage in SH-SY5Y cells.

3.6. Exemplary *in vitro* evaluation of neuroprotective biomaterials in the developed oxidative and mitochondrial stress models

To assess the functional utility of the established cellular stress models, we employed them to evaluate the neuroprotective efficacy of MPL lipid nanoparticles encapsulating MT or Quer. These biomaterial formulations were engineered with the purpose of mitigating oxidative damage, restoring mitochondrial integrity, and modulating inflammatory signaling in differentiated SH-SY5Y cells.

Characterizing the distinct, dose- and time-dependent stress responses induced by LPS, Rot, and Oli in our models enabled the identification of optimal conditions for subsequent nanoparticle evaluation. Accordingly, neurotoxic concentrations of 0.5 μM Oli and 1 μg mL^{-1} LPS were chosen to model chronic oxidative stress–induced mitochondrial dysfunction and inflammation in differentiated SH-SY5Y cells at an exposure time of 24 h. For comparison, 50 mM KPS treatment for 30 min, as described in our previous work,[25] was used to establish an acute oxidative stress model.

To evaluate the neuroprotective effects of free or MPL NPs-loaded MT and Quer, differentiated SH-SY5Y cells were subjected to oxidative and inflammatory insults. Mitochondrial activity, intracellular ROS generation, and NF-κB levels were subsequently analyzed to assess cellular recovery and stress modulation (Fig. 9).

As shown in Fig. 9A and B, exposure to 0.5 μM Oli for 24 h decreased ATP synthase activity ($p < 0.001$), confirming mitochondrial dysfunction. Pre-treatment with free MT significantly restored ATP levels. MT encapsulated in LCNPs (MPL-MT) also

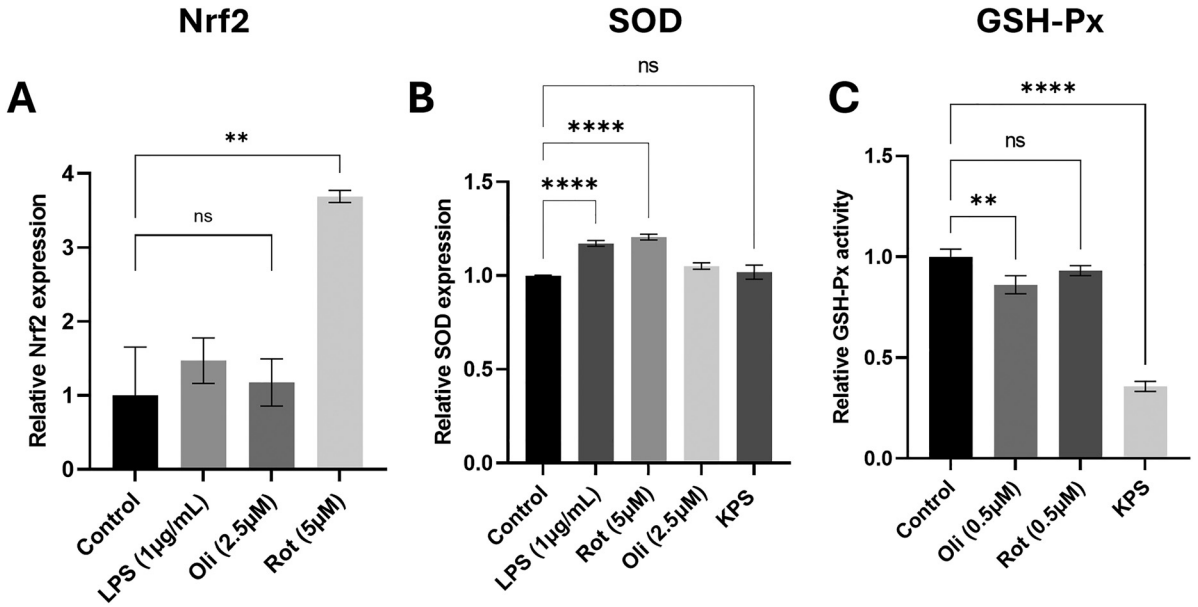

Fig. 8 Effects of LPS, Oli, and Rot on Nrf2-mediated antioxidant responses in differentiated SH-SY5Y cells. (A) Relative Nrf2 expression in LPS, Rot, and Oli-induced SH-SY5Y cells. (B) Relative SOD expression after 24 h exposure to LPS and Rot compared to unmodified expression upon exposure to Oli for 24 h or potassium persulfate (KPS, 50 mM, 30 min). (C) Relative GSH-Px activity significantly decreased after exposure to 0.5 μM Oli for 24 h and 50 mM KPS for 30 min, whereas 0.5 μM Rot caused no significant changes. Data are expressed as mean ± SD (n = 2 biological replicates). Statistical significance was determined by one-way ANOVA; $^{**}p < 0.01$, $^{***}p < 0.001$, $^{****}p < 0.0001$ *vs.* control; ns, not significant.

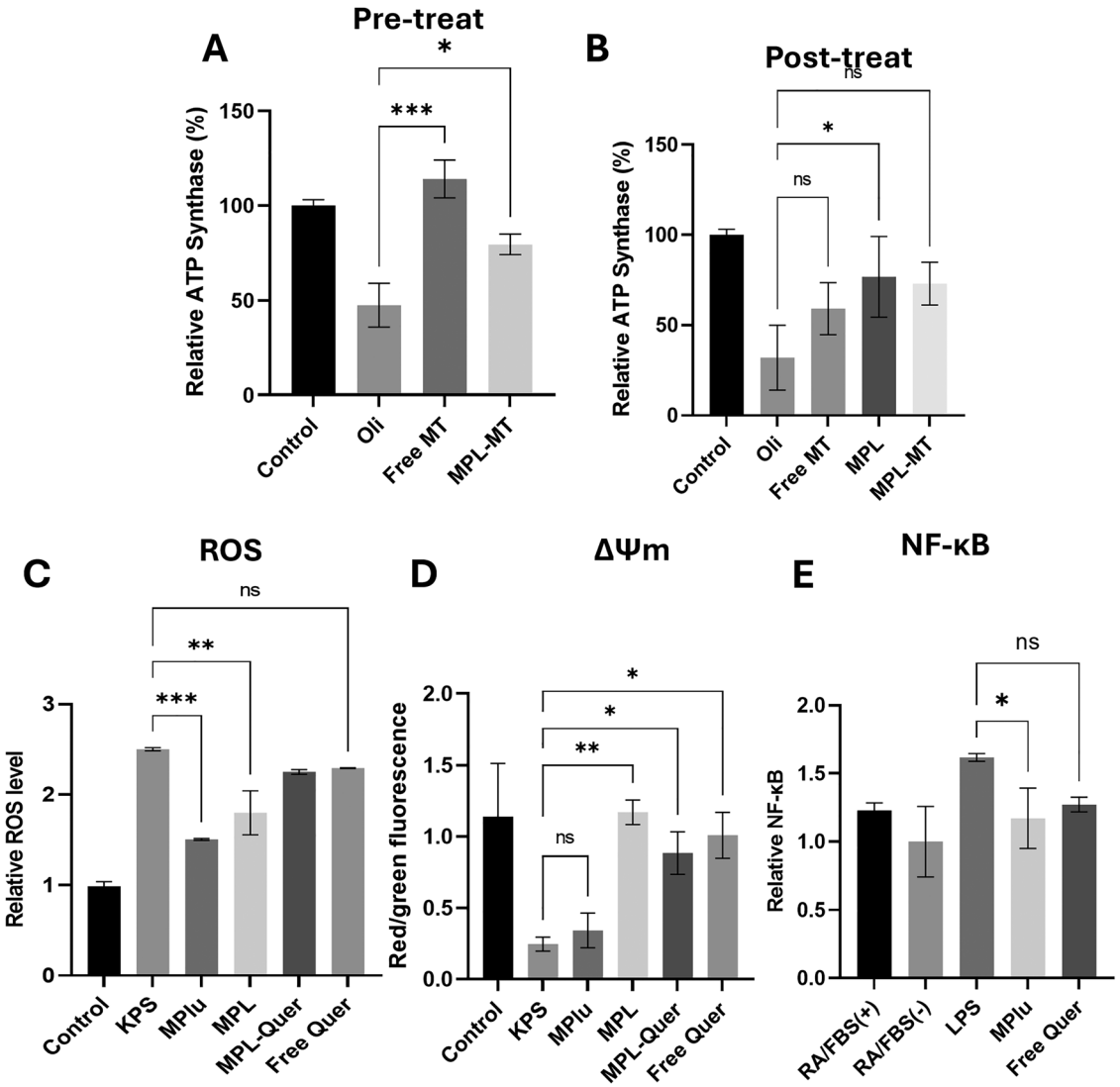

Fig. 9 Effects of chosen nanoparticulate and free drug treatments on mitochondrial activity, oxidative stress, and inflammatory response in differentiated SH-SY5Y cells. (A) and (B) Relative ATP synthase activity in SH-SY5Y cells exposed to 0.5 μM Oli, measured under pre-treatment and post-treatment conditions with free MT or MT-loaded monoolein-plasmalogen nanoparticles (MPL–MT). (C) Intracellular reactive oxygen species (ROS) levels induced by 50 mM KPS for 30 min and mitigated ROS production after treatment with liquid crystalline nanoparticles (LCNPs) or free Quer for 24 h. (D) Mitochondrial membrane potential (ΔΨm) changes, represented by the red/green fluorescence ratio measured by flow cytometry. Lower ratios after KPS exposure reflect mitochondrial depolarization, whereas treatments with LCNPs or Quer restored ΔΨm toward normal levels. (E) Increase NF-κB expression induced by 1 μg mL^{-1} LPS and modulatory effects of MPlu LCNPs and free Quer treatments. Data are presented as mean ± SD (n = 3 biological replicates). Statistical analysis was performed using one-way ANOVA, comparing each treatment group with the control. *$p < 0.05$, **$p < 0.01$, ***$p < 0.001$, ns = not significant.

enhanced ATP synthase activity, although to a slightly lesser extent than free MT. Under post-treatment conditions, both MPL and MPL-MT LCNPs exhibited stronger recovery effects than free MT, though all were less effective than pre-treatment. Interestingly, the MPL LCNPs improved ATP levels (Fig. 9B), an effect likely related to the intrinsic antioxidant and membrane-stabilizing properties of plasmalogens.[24,42] However, no clear synergistic effect was observed between MT and the MPL LCNP carriers under these conditions. These findings suggest that once oxidative damage and stress-signaling pathways are activated, mitochondrial recovery is limited, which shows that preventive treatment is more effective in preserving mitochondrial integrity under oxidative stress.

Under the acute oxidative stress conditions, stimulation with 50 mM KPS for 30 min markedly elevated intracellular ROS levels (Fig. 9C), confirming the successful induction of oxidative stress in the cells. Subsequent treatment with 1 μM LCNPs (either MPlu or MPL) for 24 h after KPS exposure significantly attenuated ROS accumulation. This suggests that the nanocarrier itself exhibits intrinsic antioxidative activity, likely arising from its amphiphilic lipid matrix and PL-based components capable of scavenging free radicals and supporting membrane stabilization or repair under oxidative stress conditions.[43–46] In contrast, both free Quer and MPL-Quer treatment only slightly mitigated ROS production under such

conditions, suggesting that at this low concentration, Quer alone cannot exert a strong antioxidant effect. Interestingly, the ROS-lowering effect of MPL-Quer was even weaker than that of the MPL LCNPs. This outcome may result from different factors, including (i) a slow or incomplete release of Quer from the LCNP matrix, limiting its active intracellular concentration, and (ii) strong interactions between Quer and lipid, which may reduce its redox accessibility and lead to quenching effects. These findings indicate that while LCNPs themselves can protect against oxidative stress, further optimization of drug loading and release kinetics will be necessary to fully exploit the antioxidant potential of encapsulated Quer in neuroprotective systems.

To further investigate the protective effects against oxidative stress–induced mitochondrial dysfunction, ΔΨm changes were assessed using the red/green fluorescence ratio as an indicator (Fig. 9D). KPS exposure significantly decreased this ratio, reflecting mitochondrial depolarisation and loss of potential. Remarkably, treatment with MPL LCNPs effectively restored the red/green fluorescence ratio toward control levels, demonstrating their strong ability to preserve mitochondrial integrity under oxidative stress. At variance, MPlu NPs showed no appreciable improvement relative to the KPS group, suggesting that the mitochondrial protection mainly originated from the PL component within the MPL formulation.

Moreover, both free Quer and MPL-Quer treatments exhibited a pronounced ability to restore ΔΨm, although MPL-Quer again showed a relatively weaker effect compared with either MPL LCNPs or free Quer. This corroborates the ROS assay results. The data obtained suggest that while Quer and PL each contribute to mitochondrial protection, their proportions in the combined formulation may require further optimization to achieve improved antioxidant performance.

Inflammation-related signaling was assessed by measuring NF-κB levels (Fig. 9E). Exposure to 1 μg mL^{-1} LPS for 24 h significantly upregulated NF-κB expression (p = 0.0003), indicating activation of inflammatory pathways. Interestingly, treatment with MPlu LCNPs markedly attenuated this activation (p = 0.0115), while free Quer also showed a mild reduction (p = 0.055). The observed suppression of NF-κB suggests that these LCNP formulations may not only counteract oxidative stress and preserve mitochondrial function but also modulate downstream inflammatory signaling. Given the known crosstalk between ROS production, mitochondrial dysfunction, and NF-κB activation,[47,48] the obtained results highlight the multifunctional protective potential of LCNP-based systems in mitigating both oxidative and inflammatory stress in neuronal environments.

4. Conclusion

Here, differentiated SH-SY5Y neuronal-like cells were employed to develop comprehensive *in vitro* models that effectively integrate oxidative stress, inflammation, and mitochondrial dysfunction, which are key pathological mechanisms underlying neurodegenerative diseases. The KPS-induced oxidative stress model demonstrated reproducible, dose-dependent ROS generation, mitochondrial impairment, and neuronal apoptosis, serving as a reliable system for mimicking oxidative injury. LPS, at an optimized concentration of 1 μg mL^{-1}, effectively activated inflammatory signaling *via* NF-κB and IL-1β pathways, whereas mitochondrial inhibitors such as Rot and Oli predominantly induced Nrf2-mediated antioxidant responses and ATP depletion, respectively. Our comparative analysis established distinct yet complementary models of neuronal stress, allowing differentiation between oxidative, mitochondrial, and inflammatory injury.

Using these *in vitro* models, MPL-LCNPs were evaluated as an exemplary neuroprotective biomaterial system, which exhibited antioxidant and mitochondrial-stabilizing properties by reducing intracellular ROS accumulation, restoring ATP synthase activity, and suppressing NF-κB expression under both oxidative and inflammatory stress. The lipid component plasmalogen played a critical role in maintaining redox homeostasis and mitochondrial integrity, while the combined loading of MT or Quer did not yield pronounced synergistic effects under the investigated conditions.

In conclusion, our work established a SH-SY5Y cell-based *in vitro* multi-model that recapitulates key features of neuronal degeneration and offers a reproducible platform for screening lipid-based neuroprotective nanomaterials targeting oxidative, inflammatory, and mitochondrial pathways.

Author contributions

The manuscript was prepared through the contributions of all authors. A. A. conceptualized and supervised the study; F. L. and T. A. contributed to the experimental investigation, data analysis, and data processing; A. A. and B. A. provided materials and resources. T. A. contributed to instrument management and software; F. L. wrote the original draft; T. A., A. A., and B. A. reviewed and edited the manuscript. All authors critically reviewed the manuscript and approved the final manuscript for submission.

Conflicts of interest

There are no conflicts to declare.

Abbreviations

6-OHDA	6-Hydroxydopamine
ATP	Adenosine triphosphate
BHT	Butylated hydroxytoluene
BSA	Bovine serum albumin
CAT	Catalase
DCFH-DA	2′,7′-Dichlorodihydrofluorescein diacetate
FBS	Fetal bovine serum
GSH-Px	Glutathione peroxidase
H_2O_2	Hydrogen peroxide

IL-1β	Interleukin-1β
IL-6	Interleukin-6
JAK/STAT	Janus kinase/signal transducer and activator of transcription
KPS	Potassium persulfate
LCNPs	Liquid-crystalline nanoparticles
LDH	Lactate dehydrogenase
LPS	Lipopolysaccharide
MAPKα	Mitogen-activated protein kinase alpha
p38 MAPKα	p38 mitogen-activated protein kinase alpha
MO	Monoolein
MPL	Monoolein-plasmalogen nanoparticles
MPL-MT	Melatonin-loaded monoolein-plasmalogen nanoparticles
MPL-Quer	Quercetin-loaded monoolein-plasmalogen nanoparticles
MPlu	Monoolein-plasmalogen-Pluronic F127 nanoparticles
MT	Melatonin
MTT	(4,5-Dimethylthiazol-2-yl)-2,5-diphenyltetrazolium bromide
NF-κB	Nuclear factor kappa B
Nrf2	Nuclear factor erythroid 2-related factor 2
Oli	Oligomycin A
PL	Plasmalogen
Plu	Pluronic F127
PUFA	Polyunsaturated fatty acid
Quer	Quercetin
RA	Retinoic acid
ROS	Reactive oxygen species
Rot	Rotenone
SOD	Superoxide dismutase
TLR4	Toll-like receptor 4
TNF-α	Tumour necrosis factor-α
ΔΨm	Mitochondrial membrane potential

Data availability

The data supporting the findings of this study are available within the article and the supplementary information (SI). Supplementary information: supplementary content for lipid nanoparticle composition and hydrodynamic nanoparticle size distribution. See DOI: https://doi.org/10.1039/d6tb00226a.

Acknowledgements

F.L. acknowledges a PhD fellowship from the China Scholarship Council. T.A. acknowledges a PhD fellowship from Campus France. A.A. acknowledges membership in the CNRS GDR2088 BIOMIM research network. B.A. and AA. thank Dr M. Drechsler for fruitful scientific collaboration. The authors thankfully acknowledge the scientific support by Dr Thomas Bizien at the SWING beamline of Synchrotron SOLEIL (Saint Aubin, France) and the allocation of beam time through project 20230326. Fig. 1 and 2A were generated with *BioRender.com*.

References

1 A. Picca, R. Calvani, H. J. Coelho-Junior, F. Landi, R. Bernabei and E. Marzetti, *Antioxidants*, 2020, **9**, 647.
2 P. Wen, Z. Sun, F. Gou, J. Wang, Q. Fan, D. Zhao and L. Yang, *Ageing Res. Rev.*, 2025, **104**, 102667.
3 S. Mani, S. Wasnik, C. Shandilya, V. Srivastava, S. Khan and K. K. Singh, *Front. Aging.*, 2025, **6**, 1615764.
4 C. Boroczky, A. Paszternak, R. Laufer, K. Tarnoczi, N. Sikur, F. Bagamery, E. Szoko, K. Varga and T. Tabi, *Int. J. Mol. Sci.*, 2025, **26**, 6581.
5 H. Xicoy, B. Wieringa and G. J. Martens, *Mol. Neurodegener.*, 2017, **12**, 10.
6 S. Påhlman, A.-I. Ruusala, L. Abrahamsson, M. E. K. Mattsson and T. Esscher, *Cell Diff.*, 1984, **14**, 135–144.
7 J. Kovalevich and D. Langford, *Methods Mol. Biol.*, 2013, **1078**, 9–21.
8 L. F. Hoffmann, A. Martins, F. Majolo, V. Contini, S. Laufer and M. I. Goettert, *Neural Regen. Res.*, 2023, **18**, 1265–1266.
9 U. C. Dash, N. K. Bhol, S. K. Swain, R. R. Samal, P. K. Nayak, V. Raina, S. K. Panda, R. G. Kerry, A. K. Duttaroy and A. B. Jena, *Acta Pharm. Sin. B*, 2025, **15**, 15–34.
10 T. Akanchise and A. Angelova, *Pharmaceutics*, 2023, **15**, 1562.
11 J. H. Chen, H. P. Ou, C. Y. Lin, F. J. Lin, C. R. Wu, S. W. Chang and C. W. Tsai, *Chem. Res. Toxicol.*, 2012, **25**, 1893–1901.
12 M. Rakotoarisoa, B. Angelov, V. M. Garamus and A. Angelova, *ACS Omega*, 2019, **4**, 3061–3073.
13 R. F. Simoes, P. J. Oliveira, T. Cunha-Oliveira and F. B. Pereira, *Int. J. Mol. Sci.*, 2022, **23**, 3009.
14 R. L. Mosley, E. J. Benner, I. Kadiu, M. Thomas, M. D. Boska, K. Hasan, C. Laurie and H. E. Gendelman, *Clin. Neurosci. Res.*, 2006, **6**, 261–281.
15 S. Qin, J. Gao, M. Ding, L. H. Vicuna and X. Wang, *Organ. Res.*, 2025, **1**, 025040006.
16 D. Merryweather, S. R. Moxon, A. J. Capel, N. M. Hooper, M. P. Lewis and P. Roach, *RSC Adv.*, 2021, **11**, 33124–33135.
17 E. De Vitis, A. Stanzione, A. Romano, A. Quattrini, G. Gigli, L. Moroni, F. Gervaso and A. Polini, *Adv. Sci.*, 2024, **11**, e2304989.
18 Y. Gu, W. Zhang, X. Wu, Y. Zhang, K. Xu and J. Su, *Clin. Transl. Med.*, 2023, **13**, e1499.
19 F. Luo, Y. Deng, B. Angelov and A. Angelova, *Biomater. Sci.*, 2025, **13**, 3421–3446.
20 M. Mehta, T. A. Bui, X. Yang, Y. Aksoy, E. M. Goldys and W. Deng, *ACS Mater. Au*, 2023, **3**, 600–619.
21 Y. Wu and A. Angelova, *Nanomaterials*, 2023, **13**, 3004.
22 X. Cai, C. J. Drummond, J. Zhai and N. Tran, *Adv. Funct. Mater.*, 2024, **34**, 2404234.
23 S. R. Cerqueira, N. G. Ayad and J. K. Lee, *Front. Cell. Neurosci.*, 2020, **14**, 576037.
24 A. Angelova, B. Angelov, M. Drechsler, T. Bizien, Y. E. Gorshkova and Y. Deng, *Front. Cell Dev. Biol.*, 2021, **9**, 617984.
25 T. Akanchise, B. Angelov and A. Angelova, *J. Med. Virol.*, 2024, **96**, e29680.

26 Y. Wu, B. Angelov, Y. Deng, T. Fujino, M. S. Hossain, T. Bizien and A. Angelova, *Adv. Ther.*, 2024, **8**, 2400093.
27 M. Rakotoarisoa, B. Angelov, M. Drechsler, V. Nicolas, T. Bizien, Y. E. Gorshkova, Y. Deng and A. Angelova, *Smart Mater. Med.*, 2022, **3**, 274–288.
28 Y. Wu, B. Angelov, Y. Deng, T. Fujino, M. S. Hossain, M. Drechsler and A. Angelova, *Commun. Chem.*, 2023, **6**, 241.
29 N. Younes, B. S. Alsahan, A. J. Al-Mesaifri, S. I. Da'as, G. Pintus, A. F. Majdalawieh and G. K. Nasrallah, *Toxicol. Res.*, 2022, **11**, 77–87.
30 F. Sivandzade, A. Bhalerao and L. Cucullo, *Bio-Protoc.*, 2019, **9**, 3128.
31 N. Li, K. Ragheb, G. Lawler, J. Sturgis, B. Rajwa, J. A. Melendez and J. P. Robinson, *J. Biol. Chem.*, 2003, **278**, 8516–8525.
32 Z. Xun, D. Y. Lee, J. Lim, C. A. Canaria, A. Barnebey, S. M. Yanonne and C. T. McMurray, *Mech. Ageing Dev.*, 2012, **133**, 176–185.
33 T. B. Sherer, R. Betarbet, C. M. Testa, B. B. Seo, J. R. Richardson, J. H. Kim, G. W. Miller, T. Yagi, A. Matsuno-Yagi and J. T. Greenamyre, *J. Neurosci.*, 2003, **23**, 10756.
34 A. Romero, J. Egea, A. G. Garcia and M. G. Lopez, *J. Pineal. Res.*, 2010, **49**, 141–148.
35 L. Y. Chung, Y. T. Lin, C. Liu, Y. C. Tai, H. Y. Lin, C. H. Lin and C. C. Chen, *Front. Pharmacol.*, 2022, **13**, 845930.
36 X. Ye, M. Zhu, X. Che, H. Wang, X. J. Liang, C. Wu, X. Xue and J. Yang, *J. Neuroinflammation*, 2020, **17**, 18.
37 R. Palorini, T. Simonetto, C. Cirulli and F. Chiaradonna, *Int. J. Cell Biol.*, 2013, 243876.
38 R. Acin-Perez, C. Beninca, L. Fernandez Del Rio, C. Shu, S. Baghdasarian, V. Zanette, C. Gerle, C. Jiko, R. Khairallah, S. Khan, D. Rincon Fernandez Pacheco, B. Shabane, K. Erion, R. Masand, S. Dugar, C. Ghenoiu, G. Schreiner, L. Stiles, M. Liesa and O. S. Shirihai, *EMBO J.*, 2023, **42**, e111699.
39 F. M. Lopes, R. Schroder, M. L. da Frota, Jr., A. Zanotto-Filho, C. B. Muller, A. S. Pires, R. T. Meurer, G. D. Colpo, D. P. Gelain, F. Kapczinski, J. C. Moreira, C. Fernandes Mda and F. Klamt, *Brain Res.*, 2010, **1337**, 85–94.
40 K. Potyrak, B. Wiatrak, E. Krzyzak, L. Szczukowski, P. Swiatek and A. Szelag, *Biomed. Pharmacother.*, 2021, **141**, 111878.
41 J. G. Lee and M. Heur, *Biol. Cell.*, 2013, **105**, 175–189.
42 J. C. Bozelli, Jr., S. Azher and R. M. Epand, *Front. Physiol.*, 2021, **12**, 730829.
43 E. V. Batrakova, S. Li, S. V. Vinogradov, V. Y. Alakhov, D. W. Miller and A. V. Kabanov, *J. Pharmacol. Exp. Ther.*, 2001, **299**, 483–493.
44 A. Pitto-Barry and N. P. E. Barry, *Polym. Chem.*, 2014, **5**, 3291–3297.
45 S. Yamashita, S. Kanno, K. Nakagawa, M. Kinoshita and T. Miyazawa, *RSC Adv.*, 2015, **5**, 61012–61020.
46 Z. Xu, A. Booth, M. Rappolt, M. Peckham, A. I. I. Tyler and P. A. Beales, *Angew. Chem., Int. Ed.*, 2025, 64, e202414970.
47 M. J. Morgan and Z. G. Liu, *Cell Res.*, 2011, **21**, 103–115.
48 M. Mittal, M. R. Siddiqui, K. Tran, S. P. Reddy and A. B. Malik, *Antioxid. Redox Signaling*, 2014, **20**, 1126–1167.